Applied Ocean Research 66 (2017) 79–94

Contents lists available at ScienceDirect

Applied Ocean Research

journal homepage: www.elsevier.com/locate/apor

Modelling 3D hydrodynamics governing island-associated sandbanks in a proposed tidal stream energy site

Antonia Chatzirodou*, Harshinie Karunarathna, Dominic E. Reeve

Zienkiewicz Centre for Computational Engineering, College of Engineering, Bay Campus, Swansea University, Fabian Way Swansea SA1 8EN, UK

ARTICLE INFO

Article history:
Received 13 June 2016
Received in revised form 26 October 2016
Accepted 10 April 2017
Available online 2 June 2017

Keywords:
Delft3D
Pentland firth
Inner sound
Tidal dynamics
Sandbanks
Tidal stream energy

ABSTRACT

A 3D numerical modelling study to investigate the existing hydrodynamic regime of the Pentland Firth Inner Sound Channel, Scotland, UK is presented. Hydrodynamics that govern some sensitive sedimentary deposits in the Inner Sound Channel are discussed. A 3D hydrodynamic model Delft3D is set up for Pentland Firth, located between Orkney Islands and mainland Scotland and a full sensitivity analysis of the numerical model is carried out. The current model set up sufficiently captures the existing hydrodynamics during a full spring-neap tidal cycle inside Pentland Firth. Using model results, the 3D structure of the dynamics of the tidal flows in the Inner Sound Channel is investigated. The temporal variability of tidal flows, the residual tidal flows in the channel and local flow interactions with the Island of Stroma are described. It is proved that the tidally dominant flows drive the sediment transport gradient model to explain the principle maintenance mechanisms of two island-associated sandbanks present in the Inner Sound. The present study provides detailed information on the physics of the tidal regime in the Inner Sound and explains the presence of sandbanks in an area of high tidal flows. Due to extremely high tidal flows, Inner Sound is considered as one of the most favourable sites for tidal energy extraction in the UK. The findings of this study will be very useful in assessing the significance of impacts of future tidal energy extraction on natural hydrodynamics and sediment dynamics of the area.

1. Introduction

In recent years marine renewable energy generation attracted the interest of energy developers and stakeholders [1]. The UK holds a leading position in the emerging marine renewable energy roadmap [2]. Among many forms of marine renewables, tidal stream energy has been identified as the most reliable and sustainable energy source. As a result, the tidal stream energy sector is a rapidly growing industry in UK waters [3]. Marine renewable energy industry is now moving towards deployment of large arrays of tidal devices. Prior to implementing large scale tidal stream turbine array installations, it is important to investigate the existing hydrodynamic regime in detail as it helps not only to understand tidal resource availability and site selection criteria but also potential environmental impacts of resource harnessing [4–6].

Pentland Firth (PF) between Scottish mainland and the Orkney Island (Fig. 1) is considered as one of the most promising locations for tidal stream energy exploitation in the UK, as a result of predominant extremely high tidal flows [7]. The complex seabed conditions, the presence of numerous islands with rugged coastlines and the highly energetic tidal regime of Pentland Firth pose an intricate hydrodynamic regime. It is important first to understand the physics of the tidal regime in the Pentland Firth in order to understand potential impacts of tidal energy harvesting. However, field measurements of any suitable quantities such as flow velocities and water levels that can be used to investigate and understand the hydrodynamics of this area are scarce. Therefore, suitable computational modelling studies that will provide detailed dynamics will be extremely useful and beneficial to renewable energy industry.

The primary aim of this study is to computationally model and investigate the 3D flow regime of the Inner Sound Channel in Pentland Firth located between north coast of Scottish Mainland and the Island of Stroma (Fig. 1). We describe the temporal variability of the tidal flows and residual tidal flows present in the channel. The local tidal flow interactions with the Island of Stroma are also examined. The results are then used to describe flow characteristics that contribute to the sustenance of two very distinct sandbanks that prevail in the area. These sandbanks are found to be a key feature of the natural sedimentary and ecological environment of the area in which the sea bed is largely sediment-free and are located at a close proximity to a proposed large scale tidal stream turbine array

* Corresponding author.
E-mail address: 684449@swansea.ac.uk (A. Chatzirodou).

http://dx.doi.org/10.1016/j.apor.2017.04.008

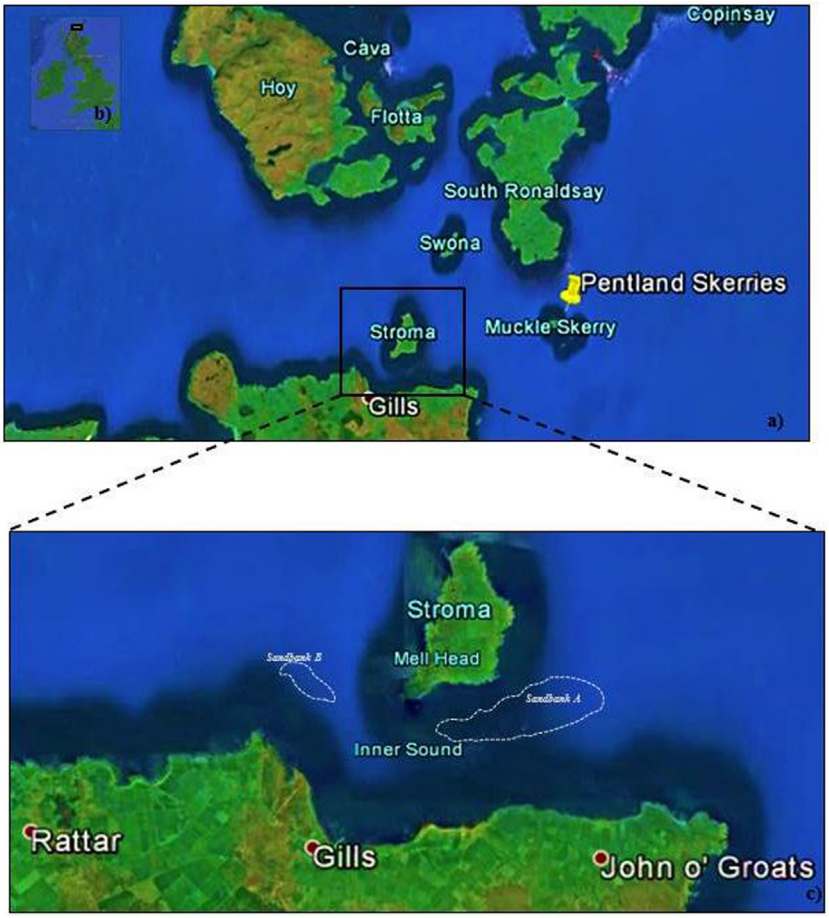

Fig. 1. a) Upper Figure: "The Pentland Firth site." 58°42′58.97″ N and 3 °06′53.47″ E. **Google Earth**. January 1, 2004. December 16, 2015; b) Upper left figure: "United Kingdom." 55°30′41.31″ and 3°21′25.69″. **Google Earth**. April 10, 2013. December 16, 2015; c) Lower Figure: "The Inner Sound channel." 58°39′23.65″ N and 3°08′21.15″ E. Google Earth. January 1, 2004. December 16, 2015. Dotted grey lines denote the extent of the two largest sandbanks A and B found in Inner Sound [8].

[8]. In Section 2 of this paper, a description of the Pentland Firth and Inner Sound Channel is given. In Section 3, the computational model is described and the sensitivity analysis of numerical model against field measurements is presented. Section 4 provides details of the most important hydrodynamic features in the Inner Sound channel. It also indicates the hydrodynamic features which mostly drive the maintenance mechanisms of two sandbanks. Section 5 concludes the paper.

2. Field Site

Pentland Firth (PF), located between Scottish Mainland and Orkney Islands joins the Atlantic Ocean and the North Sea (Fig. 1). Due to different tidal ranges and phases at the ends of the PF channel, tidal currents of up to 8 ms^{-1} are generated in places in response to 2.5 m head drop during a tidal cycle [9], providing enormous energy resource for tidal current turbines installation [10,11]. Semi-diurnal tides are predominant in Pentland Firth Channel. The highest tidal ranges are evident westwards of the channel whereas the lowest are found eastwards [4]. Maximum currents at flood phase occur towards south–south east whereas at ebb phase, tidal races travel north-westwards with a phase shift of 3 h in relation to high tides at Stromness. The jet envelope developed in a tidal cycle in between the Islands of Swona and Stroma is proved to expand further eastwards due to eastward blowing winds. At the same time, to the west, during the beginning of the flood phase, the wind forcing seems to cause a slight veering of the jet northwards [9]. Depth values vary inside the Pentland Firth channel from ~100 m in the deepest areas to less than 20 m in shallower parts closer to the coastline. Inside the Inner Sound the bathymetry decreases steadily closer to the coastline from values of up to 70 m, measured northwards. Steep bottom slopes and abrupt changes in flow depth due to the observed, narrow, submarine canyons formed between the Islands of Swona, Stroma and Muckle Skerry (see Fig. 1) create a very complex bathymetric profile in this area.

Bowyer and Marchi [9] investigated tidal residual flows in PF Channel and the mixing properties of tidal flows. They found that the fast moving tidal jet inside PF channel induces a residual dipole circulation at both ends of the channel which is proved to be more intense eastwards. The residual dipole circulation pattern is in essence a persistent vorticity field which is generated as the flow leaves the channel and is further advected away along its exits. At a turning tide the dipoles can travel further away from the channel or can be drawn back into the channel. Residual vortices along several tidal cycles are proved to play a significant role in mixing properties of tidal flows [12], which in turn may affect sediment transport processes in Pentland Firth.

Sea bed in PF is largely sediment-free. However, large patchy sand deposits lying on scoured bed rock are a common feature in some areas of PF and Inner Sound channel in particular [13]. iXSurvey (2009) observed a range of sea bed types in the Inner Sound through a Klein 3000 side-scan sonar geophysical survey [8]. Meygen [8] reported the presence of two large island-associated sandbanks, located in the lee of island of Stroma, in a deep shelf region (depths >18m), providing a clear evidence of their exact location, size and sediments characteristics (Fig. 1). Both sandbanks

are surrounded by scoured bed rock, gravel and cobble dominated areas. A detailed overview of this report is also found in Chatzirodou et al. [13]. The large, pear shaped sandbank A (Fig. 1) is located eastwards of Stroma and has maximum depth of ~30 m. It is around 3 km long with ~1 km maximum width north-eastwards. A smaller scale shelf sandbank B (Fig. 1) of 1 km length and 0.5 km width has been found westwards of Stroma at maximum depth of ~35 m. However, it should be noted that no other sediment transport or morphodynamic studies of these large morphological features have been reported other than Chatzirodou et al. [13], which provides a comprehensive sediment transport study.

3. Methodology

3.1. Numerical model description

To investigate the hydrodynamic environment in Pentland Firth Inner Sound Channel, Delft3D FLOW model [14] is used. Delft3D is a finite difference code which solves the Navier-Stokes equations under the Boussinesq and shallow water assumptions, in two (2D) or three (3D) dimensions [14]. The model is well calibrated and validated for numerous and vastly diverse coastal settings and widely used by coastal research communities around the world. For a 3D flow simulation the system of the momentum equations in −x, −y direction reads:

$$\frac{\partial u}{\partial t} + u\frac{du}{dx} + \upsilon\frac{du}{dy} + \frac{\omega}{H}\frac{du}{d\sigma} - f\upsilon = -\frac{1}{\rho_0}P_x + F_x + \frac{1}{H^2}\frac{\partial}{\partial\sigma}\left(\nu_{V,back}\frac{\partial u}{\partial\sigma}\right) \quad (1)$$

$$\frac{\partial \upsilon}{\partial t} + u\frac{d\upsilon}{dx} + \upsilon\frac{d\upsilon}{dy} + \frac{\omega}{H}\frac{d\upsilon}{d\sigma} - fu = -\frac{1}{\rho_0}P_y + F_y + \frac{1}{H^2}\frac{\partial}{\partial\sigma}\left(\nu_{V,back}\frac{\partial \upsilon}{\partial\sigma}\right) \quad (2)$$

where f is the Coriolis parameter; u and υ are the horizontal velocities in $-x$ and $-y$ direction; ω is the vertical velocity in relation to σ-coordinates [15]; $\nu_{V,back}$ is the minimum vertical eddy viscosity; P_x, P_y are the horizontal pressure terms approximated by the Boussinesq assumptions; ρ_0 is the reference water density; $H = d + \zeta$ with d the water depth below a reference level $z = 0$ and ζ the free surface elevation above that reference level and F_x, F_y are the viscous forces presenting the unbalance of the Reynold's shear stresses. For large-scale problems as in present model set up, the Reynold's stresses along the closed model domain boundaries are neglected (free-slip conditions) and viscous forces terms reduce to the Laplace operator.

Under the shallow water assumption, the vertical momentum equation reduces to the hydrostatic pressure assumption where accelerations from buoyancy terms and abrupt variations in complex topographic features are assumed to be small in comparison to gravitational acceleration. The resulting expression is:

$$\frac{\partial P}{\partial\sigma} = -\rho g H \quad (3)$$

From the integral form of Eq. (3) and for constant water density ρ, the pressure gradients in −x, −y direction read:

$$\frac{1}{\rho_0}P_x = g\frac{d\zeta}{dx} + \frac{1}{\rho_0}\frac{\mathrm{dP_{atm}}}{\mathrm{dx}} \quad (4)$$

$$\frac{1}{\rho_0}P_y = g\frac{d\zeta}{dy} + \frac{1}{\rho_0}\frac{\mathrm{dP_{atm}}}{\mathrm{dy}} \quad (5)$$

where P_{atm} is the atmospheric pressure term.

The free surface elevation ζ is computed from the depth-averaged continuity equation neglecting the contributions due to discharge/removal of water per unit surface area and evaporation/precipitation effects. So:

$$\frac{\partial\zeta}{\partial t} + \frac{\mathrm{dHU}}{\mathrm{dx}} + \frac{\mathrm{dHV}}{\mathrm{dy}} = 0 \quad (6)$$

where U and V are the depth-averaged horizontal velocities in −x and −y direction.

An Alternating Direction Implicit (ADI) time integration technique is used to solve the continuity and momentum conservation equations. The accuracy of the ADI solver depends on the Courant-Friedrich-Lewy (CFL) number. In most practical applications as in present study, the CFL number should not exceed a value of 10 but may be higher in case of small variations in space and time [16]. The horizontal advective terms in the momentum equations are discretized in space with the higher-order dissipative Cyclic scheme [17] which converges well for large time steps, where advection Courant numbers exceed unity [16].

In vertical direction, turbulent flows are resolved by applying the κ-epsilon turbulence closure model (TCM). The horizontal eddy viscosity term which represents the turbulent length scales generated by the flow in the horizontal direction is finally approached by a constant background value ($\nu_{H,back}$) and the computed, from the TCM, vertical eddy viscosity (ν_{3D}) at each σ-layer. The background eddy viscosity value ($\nu_{H,back}$) may vary with decreasing grid resolution from 1to 100 $m^2\,s^{-1}$ [16]. For further details of the Delft3D model, the reader is referred to Lesser et al. [14].

3.2. Multi-scale computational domain set up

We used the GHHS shoreline datasets (National Oceanic and Atmospheric Administration) [18], available with NGDC's GEODAS-NG software tools [19] to delimitate the land-water boundaries and generate a structured body fitted grid of variant resolution, covering the entire model domain (Fig. 2). As appears in Fig. 2, the coastline is slowly varying and therefore available shoreline resolution is assumed to be adequate for modelling purposes. Also, the areas of concern in Inner Sound, where two offshore sandbanks exist are significantly further away from the coastline. As a result, it is expected that sandbanks-associated hydrodynamics will be least impacted by the shape of the coastline, unlike in cases of nearshore sandbanks.

Initially, a large scale model covering the entire continental shelf was set up with a grid resolution of 2 km × 2 km (Domain A, Fig. 2). Spherical coordinates of the large scale model domain extend from 58°00′N to 60°00′N and from 5°44′W to 1°32′W. Open boundaries are located closer to the end of continental shelf at the western side and a few kilometres (~70 km) away from the exit of the Pentland Firth Channel in North Sea eastwards. The location of the open boundaries was chosen sufficiently far away from Pentland Firth to ensure that numerical instabilities at the boundaries will not affect the interior of the model domain. Furthermore, this selection is consistent with the analysis carried out by Adcock et al. [20] and has been demonstrated also by Serhadlıoğlu et al. [21]. In essence, it is assumed that the applied water levels at each node of an open boundary will remain unaffected due to potential tidal energy extraction in Inner Sound in future. Tidal forcing conditions along open boundaries of the large scale model were generated by the TPXO 7.2 Global Inverse Model [22], using 13 pre-selected tidal constituents. The large scale model is driven by time-varying tidal elevations along the boundaries. A high resolution model (200 m × 200 m) covering the entire Pentland Firth area was then set up (Domain B, Fig. 2). A third, very high resolution model (66 m × 66 m), which covers the Inner Sound channel of the Pentland Firth, was established in order to investigate the detailed tidal dynamics of this area (Domain C, Fig. 2). The three domains run in a coupled mode and communicate along internal boundaries (Fig. 2). This numerical technique, referred as domain decomposition, can be regarded as an on-line, two-way nesting procedure. Domains are allowed to exchange information of momentum and continuity equations along the coupled boundaries at each computational time step, as in case of a single fully unstructured grid set

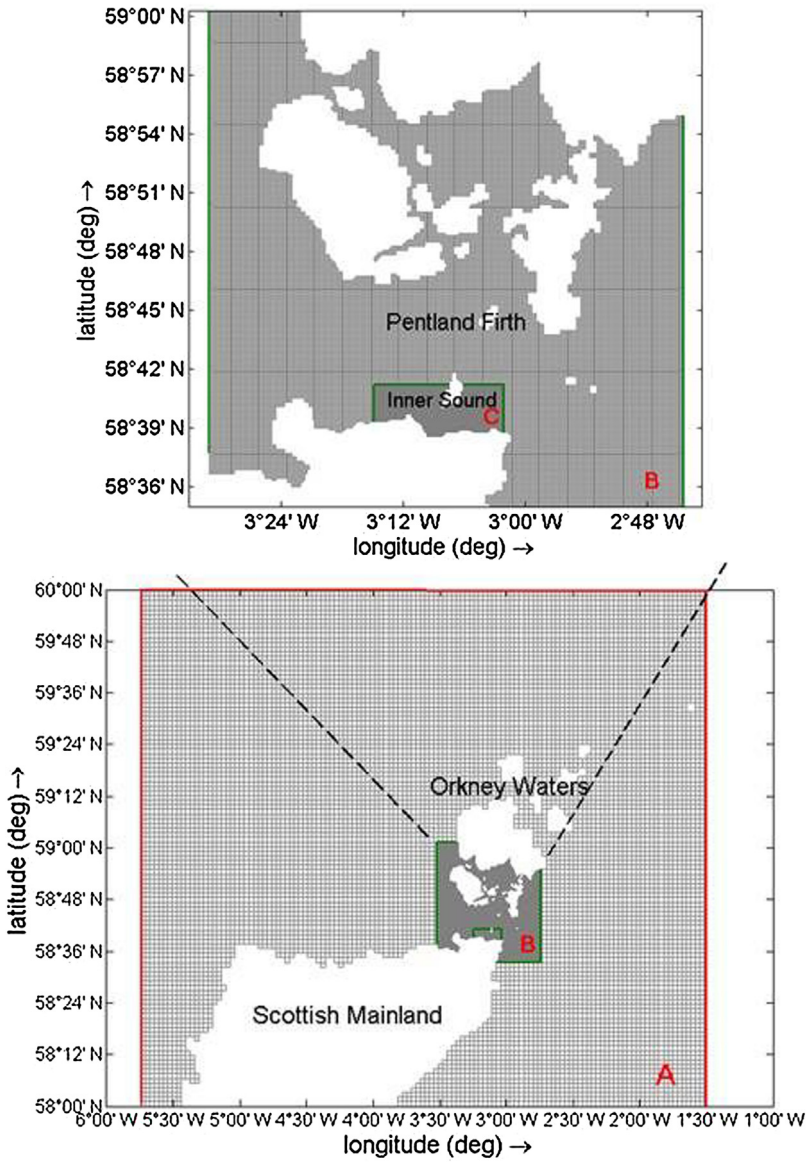

Fig. 2. Multi-scale computational domain set up. A: Large scale model covering the entire continental shelf (2 km × 2 km), B: Pentland Firth model (200 m × 200 m), C: Inner Sound channel model (66 m × 66 m). Red lines denote the open boundaries and green lines denote the coupled internal boundaries used in domain decomposition process. (For interpretation of the references to color in this figure legend, the reader is referred to the web version of this article.)

up. In the horizontal direction, each grid cell in the coarse domain corresponds to an integer number of grid cells in the adjacent refined domain. The same rule applies for vertical grid refinement where each σ-layer thickness in the coarse domain equals to the total layer thicknesses of the corresponding layers in the refined domain [16].

Following Baston et al. [23], a 2D formulation of Delft3D flow model was run for the shelf-scale domain (Domain A) in a fully coupled mode with the 3D higher resolution model (Domain B). Domain C is set up in a 3D fully coupled mode along internal boundaries, with Domain B. The same time step of 0.20 min has been applied in all three domains. It is worth noting that the spatial, in horizontal direction, and temporal resolution were selected based on their dependency on the CFL number limitation ($\leq$10) and refined to an extent which allowed best possible representation of hydrodynamics in all model domains (A, B, C).

Lastly, the model bathymetry data were provided by The Crown Estate (TCE), UK through the Terawatt project funded by the Engineering and Physical Science Research Council, UK, at a very fine grid resolution of 20 m × 20 m (Fig. 3).

3.3. Sensitivity analysis of the numerical model

A sensitivity analysis of the Delft3D flow numerical model used in this study was carried out using flow measurements available at three different sites in Pentland Firth. The measurements have been conducted between 14/09/2001 and 20/10/2001 by the Oceanography Department of Gardline Surveys, using seabed Acoustic Doppler Current Profiler (ADCP) gauges (Fig. 4). The details of the ADCP measurements can be found in Baston et al. [23] and Adcock et al. [24]. It was found that overall model outputs were significantly sensitive only to bed friction. Thus, sensitivity analysis results of the Chézy bed friction coefficient, which was taken as a constant over the model domain, will only be presented and discussed in detail here. It should be noted that due to lack of detailed information of the sea bed in the Pentland Firth, investigation of a spatially varying friction coefficient was not possible. We will

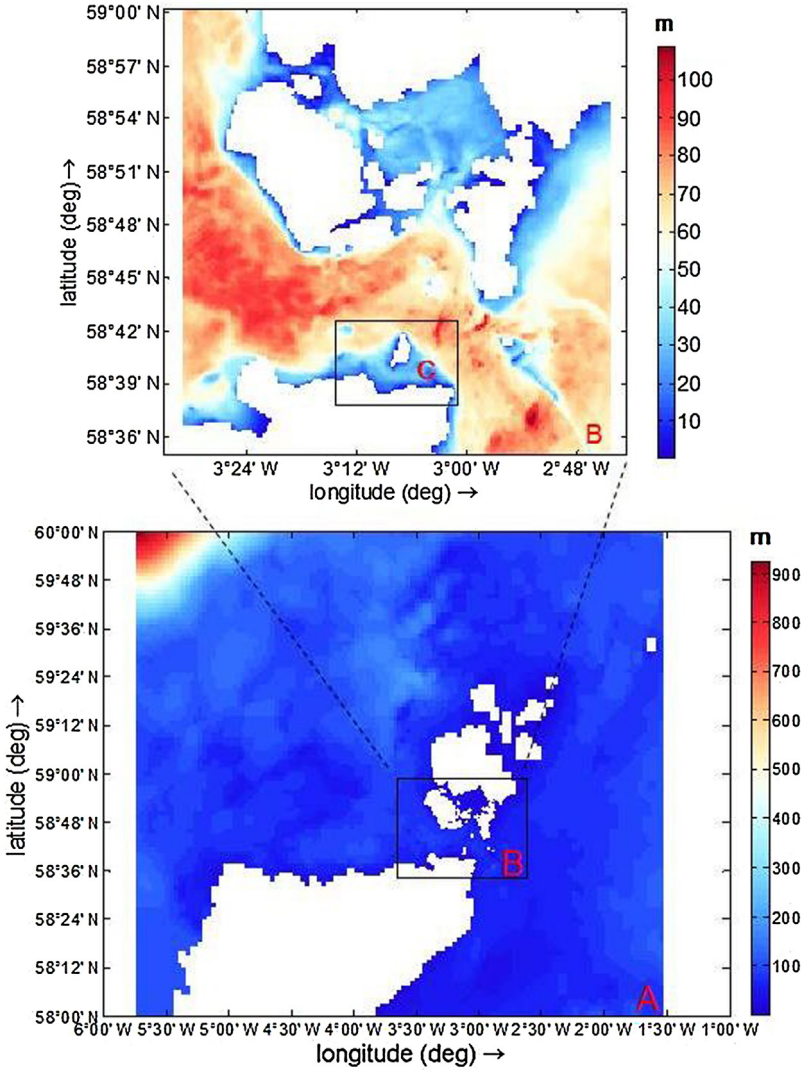

Fig. 3. Numerical bathymetry generation. The hydrodynamic grids (A, B, C) are mapped onto bathymetry data available at 20 m × 20 m grid resolution. The colour bars indicate the water depth values (m).

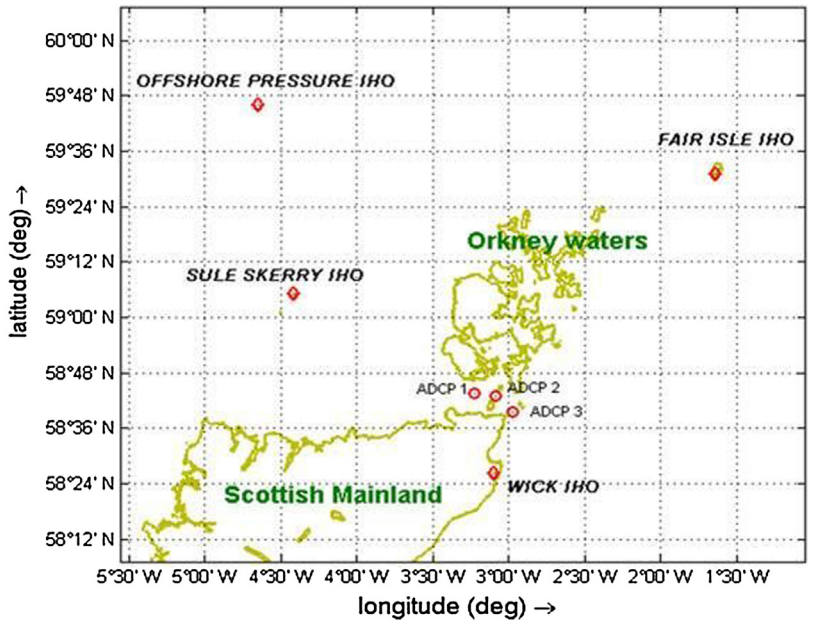

Fig. 4. Study area with the location of three ADCP Sites and four IHO tidal gauges.

Table 1
Root Mean Square Error (RMSE) (m/s) between measured and modelled horizontal velocities (m/s) in the vertical column at ADCP sites 1, 2 and 3 at maximum neap (26/09/2001) and spring (04/10/2001) tide, for the Chézy coefficient of 40,50,60 $m^{(1/2)}\,s^{-1}$.

a.

ADCP 1	RMSE (m/s)		
Chézy value ($m^{(1/2)}\,s^{-1}$)	40	50	60
Neap Tide-Ebb	0.08	0.28	0.26
Neap Tide-Flood	0.03	0.08	0.13
Spring Tide-Ebb	0.69	0.34	1.01
Spring Tide-Flood	0.22	0.05	0.26

b.

ADCP 2	RMSE (m/s)		
Chézy value ($m^{(1/2)}\,s^{-1}$)	40	50	60
Neap Tide-Ebb	0.06	0.16	0.43
Neap Tide-Flood	0.14	0.04	0.14
Spring Tide-Ebb	0.28	0.28	0.70
Spring Tide-Flood	0.30	0.12	0.46

c.

ADCP 3	RMSE (m/s)		
Chézy value ($m^{(1/2)}\,s^{-1}$)	40	50	60
Neap Tide-Ebb	0.24	0.21	0.31
Neap Tide-Flood	0.28	0.04	0.44
Spring Tide-Ebb	0.32	0.24	0.14
Spring Tide-Flood	0.24	0.74	1.46

briefly discuss the selection procedure of other model parameters, which had minimal impacts on model outputs.

Chézy coefficient represents the friction losses due to the interaction of tidal currents and rough sea bed. Friction losses along with turbulence contribute to natural dissipation of a significant amount of energy in the ocean. For current only flows, the bottom shear stress is given by a quadratic friction law which is in 3D form reads as:

$$\vec{\tau}_{b3D} = \frac{g\rho_o|\vec{u_b}|\vec{u_b}}{{C_{3D}}^2} \tag{7}$$

In Eq. (7), $|\vec{u_b}|(ms^{-1})$ is the horizontal velocity component which is assigned to the first computational layer above the seabed. The prescribed value of a constant Chézy coefficient C_{3D} ($m^{(1/2)}\,s^{-1}$) applied in Eq. (7), results in a dimensionless bottom friction coefficient in accordance to the $\left(\frac{g}{{C_{3D}}^2}\right)$ relationship. Higher Chézy values represent a smoother bed whereas lower values represent a rougher bed.

Various statements can be found in literature on the selection of the dimensionless friction coefficient for Pentland Firth; Pugh [25] suggests a typical value of 2.50×10^{-3} for Shelf Sea flows, whereas Salter [26] denotes that 8.60×10^{-3} is a more appropriate value. Adcock et al. [24] used a constant value of 5×10^{-3} following Baston and Harris [11]. However, Easton et al. [27] concluded, using a 2D model based on MIKE21 that a constant bed friction value of 0.0035 applied to the Inner Sound Channel, resulted in a better output for the current velocity field, against measurements during spring tides.

Three different Chézy values 40, 50, 60 $m^{1/2}\,s^{-1}$; equaling to dimensionless coefficients of 6.25×10^{-3}, 4×10^{-3}, 2.8×10^{-3} respectively were tested. Fig. 5 provides a detailed comparison between the modelled and measured horizontal velocities in the vertical column at the three ADCP locations: at the ebb and flood phases of the highest neap (26/09/2001), spring tides (04/10/2001), and for all three Chézy values. The model reproduced the general form of the horizontal velocity profiles in the water column at all three sites. However, the Chézy coefficient of 60 $m^{1/2}\,s^{-1}$ appears to overpredict the velocity magnitudes while 40 $m^{1/2}\,s^{-1}$ tends to underpredict them. Overall, the Chézy coefficient of 50 $m^{1/2}\,s^{-1}$ provided the best fit between measured and simulated velocity profiles, although a few deviations are observed in Sites 1 and 3. Using the same ADCP records; Baston et al. [23] carried out Delft 3D flow sensitivity analysis on a coarser domain configuration and observed similar deviations in Sites1 and 3. They claimed these deviations may be attributed to the fact that the model did not sufficiently resolve the turbulent flows which bypass the narrow strait between the Islands of Stroma and Swona and, then suddenly expand and decelerate further downstream. Despite the fact that a more refined domain is used here it seems that the present model setup also does not sufficiently resolve these same turbulent plume characteristics at sites 1 and 3. However, for the purposes of this study where the focus is on hydrodynamics linked to the existence of sandbanks, the model resolution was assumed adequate.

To support observations in Fig. 5, the Root Mean Square Error (RMSE) values between measured and simulated horizontal velocity profiles, at maximum ebb and flood phases throughout the spring-neap cycle were then calculated (Table 1). For the best fitted Chézy value of 50 $m^{1/2}\,s^{-1}$, a maximum RMSE was 0.7 ms^{-1} at Site 3, at peak spring flood phase (04/10/2001 9:20). However, for all other cases RMSEs of Chézy 50 $m^{1/2}\,s^{-1}$ are below 0.3 ms^{-1}.

The background horizontal eddy viscosity ($\nu_{H,back}$), the vertical layer distribution profile and the number of vertical layers are the other important parameters that were tested but did not influence model's ability to predict the flow regime accurately. A range of $\nu_{H,back}$ values from 1 to 100 m^2s^{-1} were tested in Domains A, B and C. However, predictions of horizontal velocities in the vertical column at 3 ADCP sites proved to be almost insensitive for all tested values. As a result, a minimum uniform value of 10, 5 and 1 m^2s^{-1} was assigned in Domains A, B and C respectively to account for any smaller-scale than grid size unresolved turbulent eddies. To increase the efficiency of the solution procedure in 3D model simulations and to maintain computation times at acceptable levels a compromise needs to be made between the number and the vertical structure of the selected σ-layers. After a number of sensitivity tests which least influenced modelled outputs and following recommended values by Lesser et al. [14], 10 equidistant σ-layers were used in the present study. All key model parameters–described in

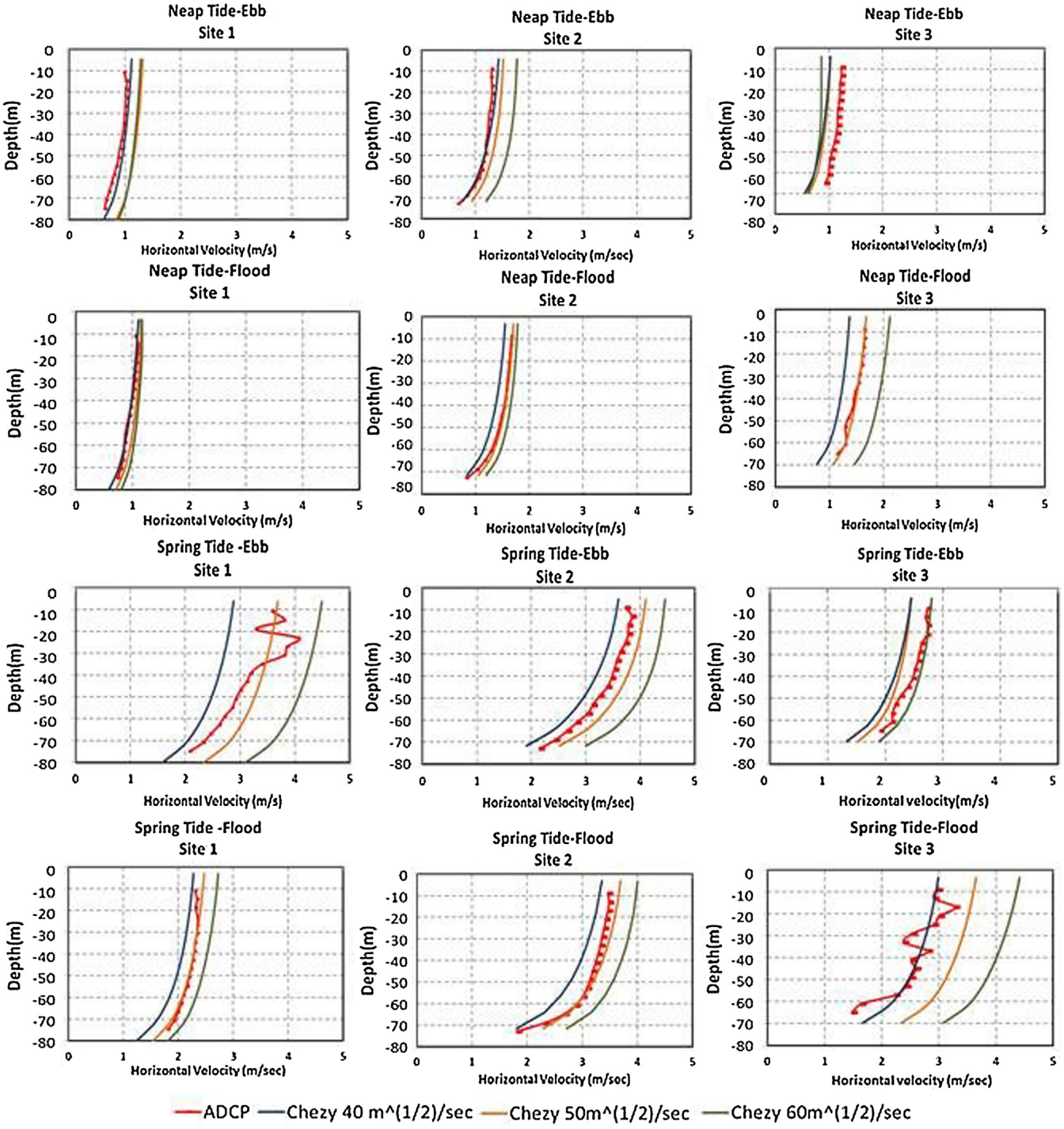

Fig. 5. Comparisons of the horizontal velocities (m/s) in the vertical column between measured and modelled flows, at 3 ADCP sites at maximum neap (26/09/2001) and spring (04/10/2001) tide and for three Chézy coefficients, 40, 50 and 60 $m^{(1/2)}\ s^{-1}$.

Sections 3.1, 3.2, 3.3 that have been used for the representation of hydrodynamics in the Pentland Firth, Inner Sound channel are finally summarized in Table 2.

Further tests on the performance of the model with selected key parameters (Table 2) were carried out in order to consolidate and justify the selected values. Horizontal velocities calculated at three ADCP sites are first compared with the measured values for a full neap-spring cycle, between 26/09/2001 and 4/10/2001 and at three depths below the mean water surface (Fig. 6). As can be seen in Fig. 6, best agreement in comparisons is found in middle depth layers at all three sites. Few deviations are seen in upper and lower layers at peak ebb and flood phases throughout the neap-spring cycle, where the maximum RMSE was found to be 0.42 ms^{-1} in Site 1 at the surface layer, which is less than 10% of the actual peak velocity. A dimensionless skill index (d) [28] was also calculated

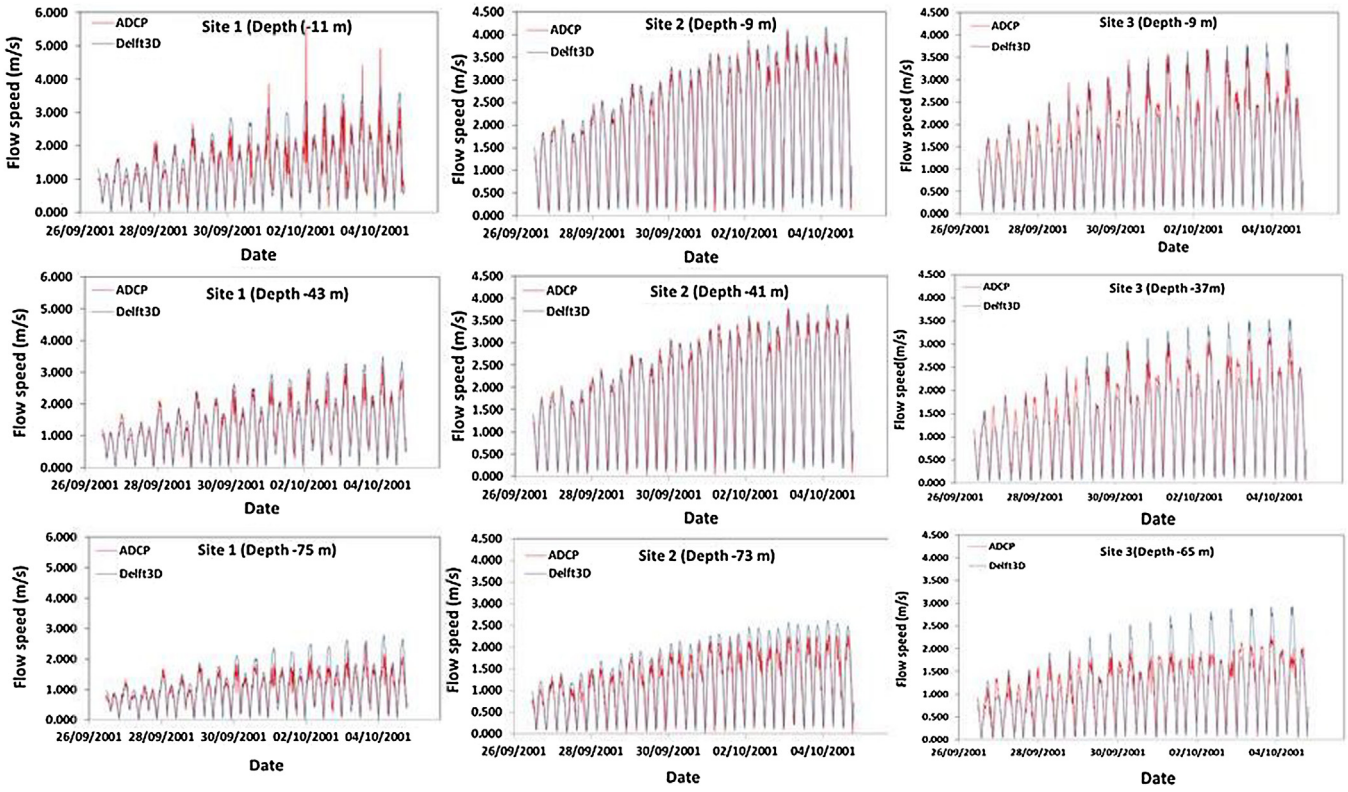

Fig. 6. Comparisons of horizontal current velocity (m/s) time-series at three depths below the mean water surface, between measured and modelled flows over a full neap (26/09/2001)-spring (04/10/2001) tidal cycle, for the selected Delft3D flow key parameters.

Table 2
Delft3D flow key parameters selected to model the hydrodynamics of the study area.

Key Parameter	*Value*
Grid size	Domain A: 2 km × 2 km (2D) Domain B: 200 m × 200 m (3D) Domain C: 60 m × 60 m (3D)
Grid elements	Domain A: 11168 Domain B: 33978 Domain C: 14382
Vertical distribution profile	even σ-layers
No. of vertical layers	10
Time step	0.2 min
Open boundary conditions	Astronomical water elevations (13 constituents)
Slip conditions (wall roughness)	Zero tangential shear stress (free slip)
Chézy bed friction	50 $m^{1/2} s^{-1}$
Initial boundary conditions	Surface elevation & velocity=0
Background horizontal eddy viscosity $\nu_{H,back}$	Domain A: 10 $m^2 s^{-1}$ Domain B: 5 $m^2 s^{-1}$ Domain C: 1 $m^2 s^{-1}$
Density	barotropic
Turbulence Closure Model (TCM)	κ-epsilon

to measure the degree to which the simulated flow time-series are error-free (Table 3):

$$d = 1 - \frac{\sum_{i=1}^{N} (P_i - O_i)^2}{\sum_{i=1}^{N} \left[|P_i'| + |O_i'| \right] 2} \quad (8)$$

Table 3
Root Mean Square Error (RMSE) (m/s) and Skill index (d) between measured and modelled time series of horizontal current velocity at three depths below the mean water surface, at 3 ADCP sites over a full neap (26/09/2001)-spring (04/10/2001) tidal cycle, for the selected Delft3D flow key parameters.

ADCP sites		RMSE (m/s)	SKILL INDEX (d)
SITE 1	Depth −11 m	0.42	0.921
	Depth −43 m	0.26	0.968
	Depth −75 m	0.30	0.923
SITE 2	Depth −9 m	0.27	0.984
	Depth −41 m	0.24	0.986
	Depth −73 m	0.29	0.951
SITE 3	Depth −9 m	0.31	0.970
	Depth −37 m	0.27	0.973
	Depth −65 m	0.33	0.926

where N equals to the total number of values compared; P_i denotes the predicted value from the computational results; O_i denotes the observed value; $P_i' = P_i - \overline{O}$ and $O_i' = O_i - \overline{O}$. It is assumed that the P_i, O_i magnitudes that are not in error equal to $\overline{O}$, since $\overline{O}$ is considered to be error-free. The skill index value may vary from 0 to 1. A skill index close to unity reflects more accurate estimates of the computed variable. A minimum skill index of 0.921 has been computed in Site 1 at the surface layer. These results show that the selected parameters (Table 2) are suitable to model the hydrodynamics of the study area and that the model is able to capture the dynamics of tidal flows very satisfactorily.

In Fig. 7 the direction of measured and simulated ebb and flood currents for the neap (26/09/2001)-spring (4/10/2001) tidal cycle is compared at all three sites. The comparison is made at same three depths below the mean water surface. A slight veering of currents is observed throughout the water column. A directionality offset between modelled and predicted directions is more pronounced at

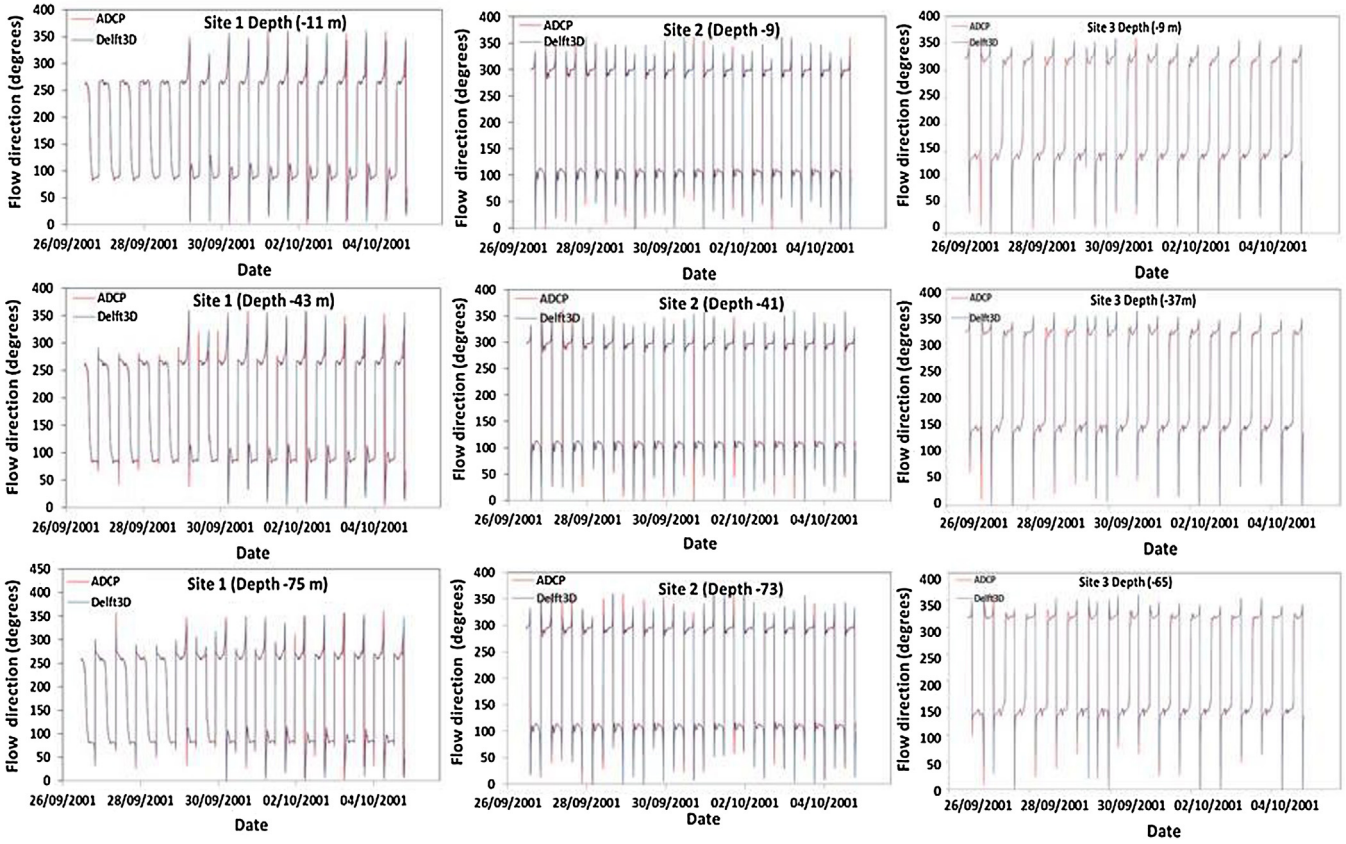

Fig. 7. Comparisons of horizontal current direction (degrees) time-series at three depths below the mean water surface, between measured and modelled flows over a full neap (26/09/2001)-spring (04/10/2001) tidal cycle, for the selected Delft3D flow key parameters.

Table 4
Root Mean Square Error (RMSE) (degrees) and Skill index (d) between measured and modelled time series of horizontal current direction at three depths below the mean water surface, at 3 ADCP sites over a full neap (26/09/2001)-spring (04/10/2001) tidal cycle, for the selected Delft3D flow key parameters.

ADCP sites		RMSE (degrees)	SKILL INDEX (d)
SITE 1	Depth −11 m	33.59	0.967
	Depth −43 m	33.15	0.968
	Depth −75 m	33.73	0.967
SITE 2	Depth −9 m	15.32	0.994
	Depth −41 m	20.75	0.989
	Depth −73 m	21.26	0.988
SITE 3	Depth −9 m	15.32	0.993
	Depth −37 m	11.75	0.999
	Depth −65 m	16.80	0.999

Table 5
Root Mean Square Error (RMSE) (m) and Skill index (d) between measured and modelled time series of water levels, at 4 IHO tidal gauges over a full neap (26/09/2001)-spring (04/10/2001) tidal cycle, for the selected Delft3D flow key parameters.

TIDAL GAUGES (IHO)	RMSE (m)	SKILL INDEX (d)
WICK	0.07	0.991
FAIR ISLE	0.06	0.982
SULE SKERRY	0.07	0.993
OFFSHORE PRESSURE	0.03	0.998

maximum ebb and flood phase throughout the neap-spring cycle. Larger angles correspond to ebb phase whereas smaller angles to flood phase (Fig. 7). As can be seen in Table 4 where the RMSE and skill index values have been calculated between measured and predicted flow directions at the three depth layers, maximum deviations are in the lower layer at all three sites. The maximum RMSE was found to be 33.73° with minimum skill index of 0.967 at the lower layer in Site 1. Overall and despite few deviations, the predicted directions are in a very good agreement with the measured values. Both for the velocity magnitude and direction (Figs. 5 and 6), the model's performance against measurements varied throughout the water column which proves the importance of carrying out a 3D modelling study in the area of interest, based on the availability of data. Model domains communicate information through internal boundaries which means that a best possible representation of hydrodynamics in Pentland Firth, where ADCP data are available, allows a better representation of flows in Inner Sound channel. A well calibrated model will resolve with higher accuracy the tidally-dominant sandbanks dynamics in Inner Sound and also allow best possible representation of tidal energy extraction in the water column, in the channel in future applications.

To demonstrate the ability of the model with selected key parameters (Table 2) to effectively reproduce large-scale hydrodynamics of Pentland Firth channel, the measured water surface elevations at four IHO (International Hydrography Organization) locations, SULE SKERRY, OFFSHORE PRESSURE, FAIR ISLE and WICK (Fig. 4), were compared with predicted elevations. Water level predictions, located in Domain A were taken from the tide station toolbox in the Delft Dashboard model interface [29] which covered a time period between 26/09/2001 and 04/10/2001.

A good agreement is found between the measured and predicted water levels both in phase and amplitude at all four sites (Fig. 8), with a RMSE value of less than 0.07 m and a Skill index very close to unity (Table 5). Unfortunately, tidal current velocities are not available at these sites. The results presented in this section reveal

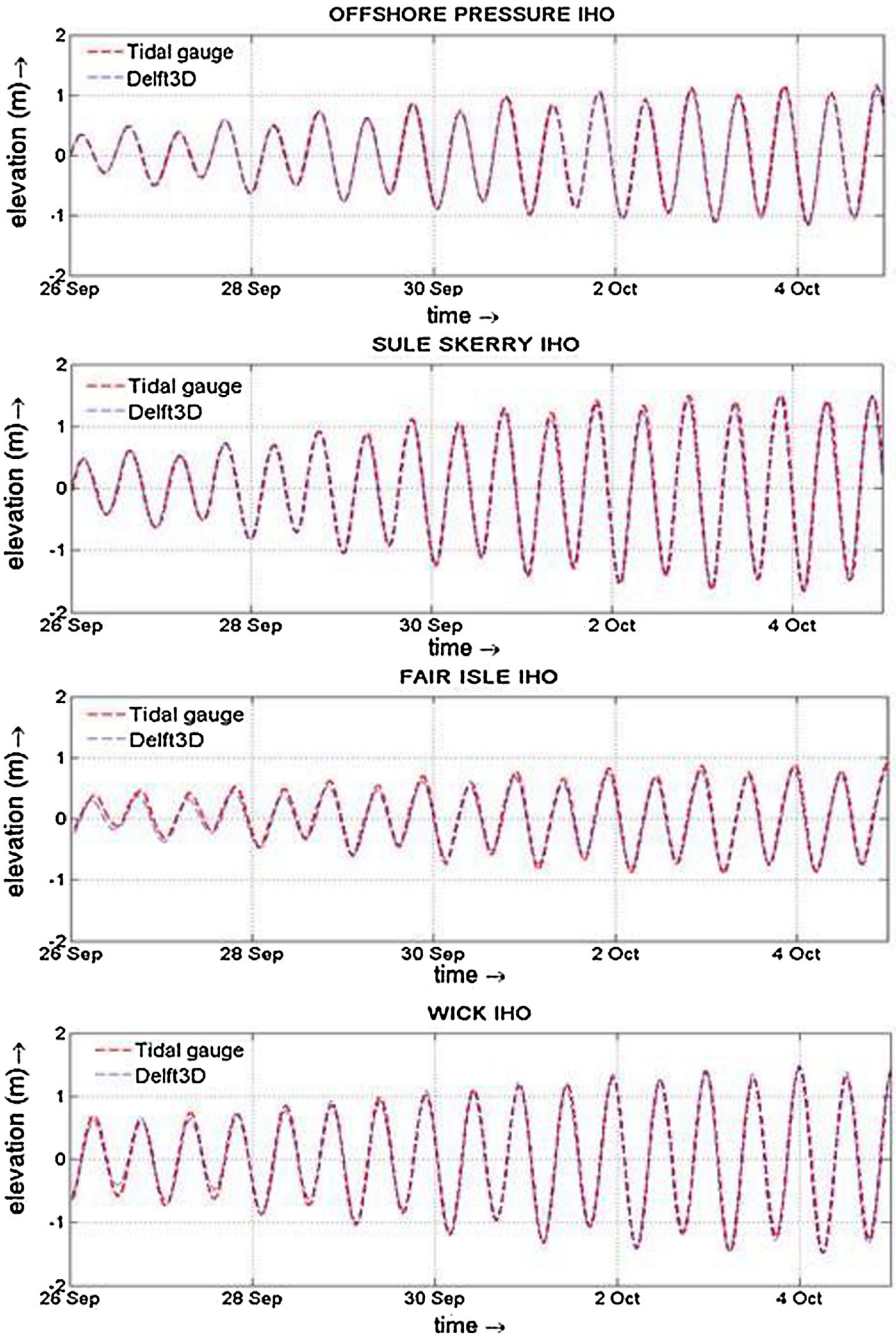

Fig. 8. Comparisons between measured and modelled surface elevations (m), at 4 IHO tidal gauges over a full neap (26/09/2001)-spring (04/10/2001) tidal cycle, for the selected Delft3D flow key parameters.

that the model is able to capture essential hydrodynamics of the selected study area.

4. Description of the tidal physics inside Inner Sound channel

In this section, the application of the model to investigate the detailed hydrodynamics of the Inner Sound Channel will be described at spring tide 04/10/2001, using 3D simulations covering a full neap-spring tidal cycle between 26/09/2001 00:00 and 04/10/2001 24:00. Main flow features that contribute to the existence and sustenance of two large sandbanks found in Inner Sound (see Section 2) will be discussed here as well.

4.1. Temporal variability of tidal flows

At maximum ebb phase, (04/10/2001 3:20), strong currents form a tidal jet reaching a speed of more than 4.3 ms^{-1} and 2.9 ms^{-1} at the surface and bottom layer, closer to island's tip (Fig. 9). The jet travels offshore from the western side of the island (Fig. 9), and exits Inner Sound from the North West, with ~200° to 250° flow direction. Three hours later, at slack water time (04/10/2001 06:00) currents start to flow parallel to the western side of Stroma. At Mell Head, closer to island's tip, flow turns to follow the coastline. At the eastward side of Stroma weak currents of up to ~0.2 ms^{-1}, at the surface layer are still ebbing. At maximum flood phase, (04/10/2001 09:20), flow has completely reversed and currents flow towards

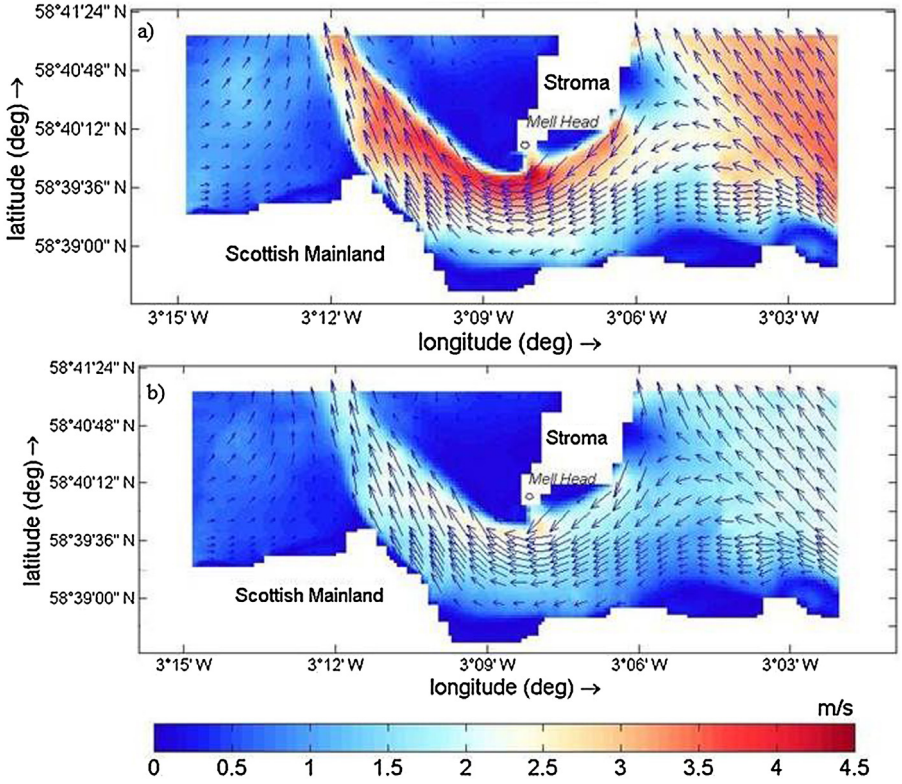

Fig. 9. Horizontal velocity (m/s) at the a) surface and b) bottom layer, at maximum spring ebb tide (04/10/2001 03:20) inside the Inner Sound channel. The colour bar indicates the magnitude of velocity and arrows indicate velocity direction.

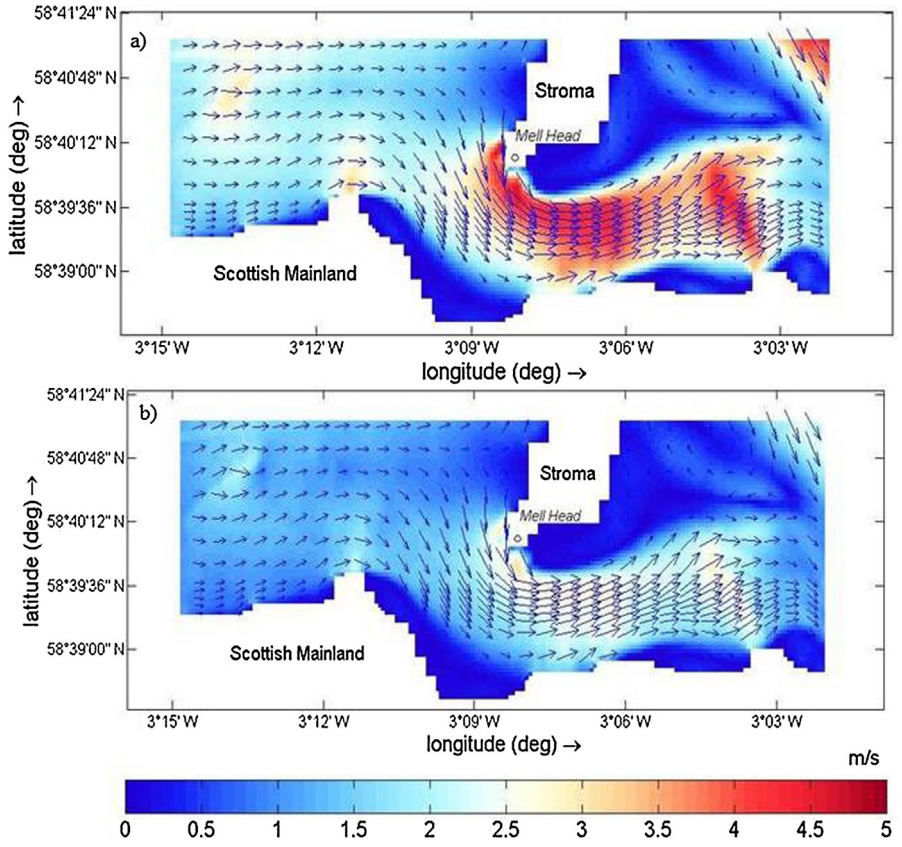

Fig. 10. Horizontal velocity (m/s) at the a) surface and b) bottom layer, at maximum spring flood tide (04/10/2001 09:20) inside the Inner Sound Channel. The colour bar indicates the magnitude of velocity and arrows indicate velocity direction.

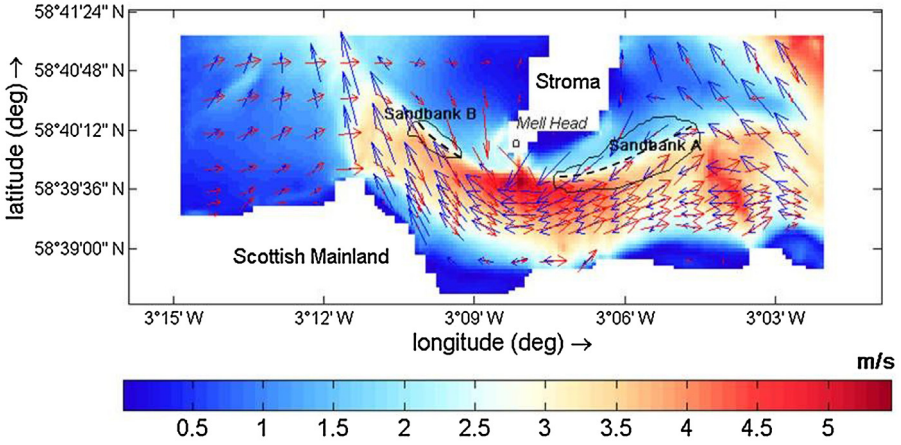

Fig. 11. Differences between maximum spring ebb (04/10/2001 03:20) and flood (04/10/2001 09:20) horizontal velocity (m/s) at the bottom layer. The colour bar indicates the difference in velocity magnitude. Blue arrows indicate maximum spring ebb velocity vector and red arrows indicate maximum spring flood velocity vector. Black continuous lines denote the location of sandbanks A and B. Dashed black lines indicate central sandbank areas where less strong symmetrical currents occur. (For interpretation of the references to color in this figure legend, the reader is referred to the web version of this article.)

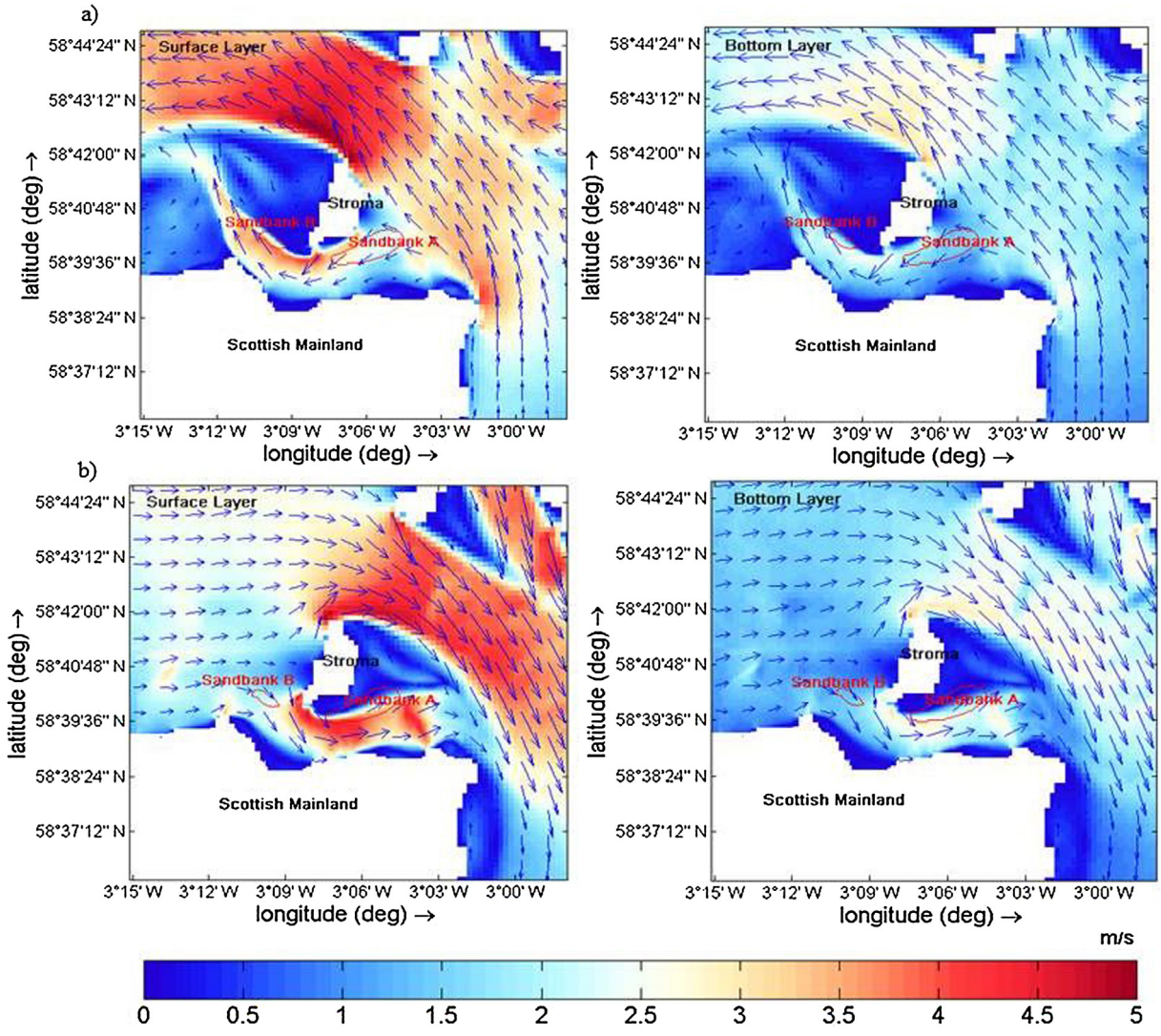

Fig. 12. Circular flow patterns (m/s) at the surface and bottom layer in the west and east wake region of the Island of Stroma at maximum spring a) ebb (04/10/2001 3:20) and b) flood phase (04/10/2001 09:20) (deep blue areas). The colour bar indicates the magnitude of velocity and arrows indicate velocity direction. Red continuous lines denote the location of sandbanks A and B. (For interpretation of the references to color in this figure legend, the reader is referred to the web version of this article.)

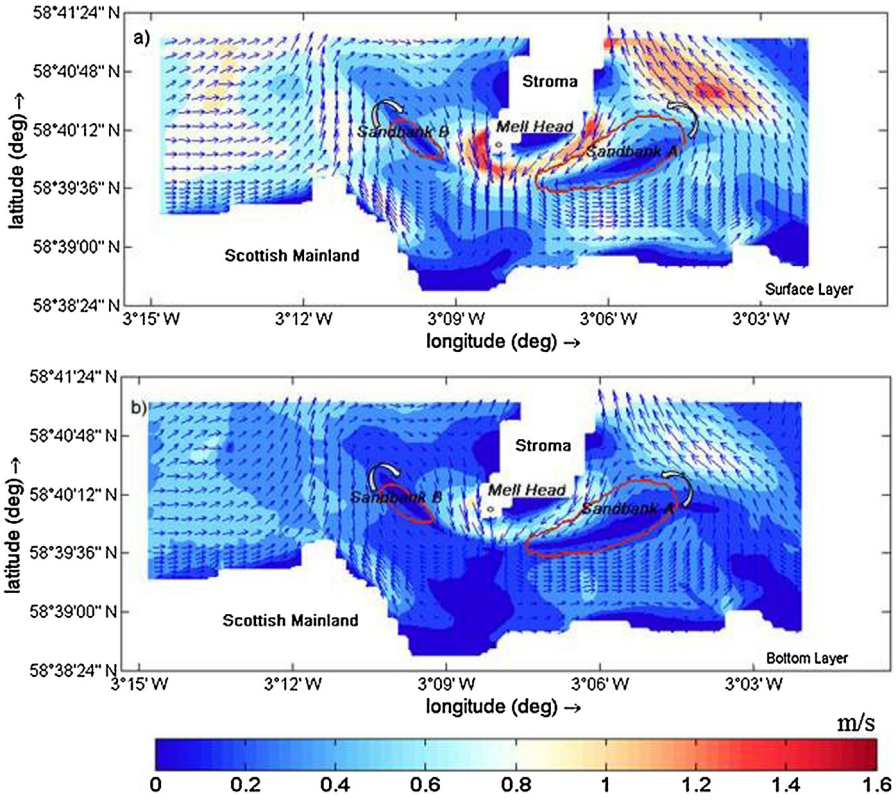

Fig. 13. Residual velocities (m/s) at the a) surface and b) bottom layer inside the Inner Sound channel for a full spring tidal cycle (04/10/2001) (white arrows indicate the rotational direction of residual current eddies-red continuous lines denote the location of sandbanks A and B). The color bar indicates the magnitude of velocity and blue arrows indicate velocity direction. (For interpretation of the references to colour in this figure legend, the reader is referred to the web version of this article.)

the east-northeast direction. They tend to veer moderately offshore from the southern-most side of Stroma, whereas flows reach a maximum velocity of up to 4.7 ms^{-1} and 3.1 ms^{-1} at the surface and bottom layer, closer to island's tip (Fig. 10). In a similar manner to ebb phase, a fast moving tidal jet forms in the middle part of Inner Sound channel. Closer to the end of flood phase (04/10/2001 11:20) a weaker tidal jet is still flowing north-eastwards where surface flow velocities reach a maximum of ~2.6 ms^{-1} at the eastern side of the jet. For supplementary information readers are referred to Videos 1 and 2 (see Supplementary Table 1 in the online version at DOI: 10.1016/j.apor.2017.04.008)–available with electronic version– where a full visualization of the tidal flows at the surface and bottom layer in between maximum flood and ebb phases is provided.

Over the tidal cycle current patterns vary in similar manner throughout the water column, as can be seen in Figs. 9 and 10 (see also supplementary Videos 1, 2 available with electronic version). Despite similarities in flow patterns at all depths, currents in the bottom layer are consistently offset relative to current vectors in the surface layer. Results also show that the direction of offset is the direction of the rotation of the surface current vectors relative to north, at each phase of the tidal cycle. Such finding can be important when modelling sandbanks dynamics in Inner Sound –in future applications– where bottom currents dominate sediment motions, underpinning the importance of carrying out 3D model runs in present study.

The presence of strong bottom currents in the tidal jets both at ebb and flood phase justifies the scoured rocky sea bed structure covering most parts of the Inner Sound channel. However the strength and directionality of the observed tidal jets (Figs. 9 and 10) are uneven when compared between the two tidal phases, as can be seen in Fig. 11, where the differences between maximum bottom ebb and flood currents have been calculated. These results are consistent with the results produced by Easton et al. [27] and Goddijn-Murphy et al. [30] and indicate a significant asymmetry between maximum ebb and flood currents in few areas around the two sandbanks (A, B). Less strong symmetrical currents occur, and create sheltered regions inside the channel over the tidal cycle, which mostly coincide with central parts of sand accumulation areas (A, B) (Fig. 11).

4.2. Tidal flows interaction with the Island of Stroma

The width to length (w/l) ratio of the island and the asymmetric geometry of the island's tip control the intensity of circular flow patterns which form in an island's wake region. Less intense circular flows can be found in places where w/l ratios are greater than 0.25, as is the case of Stroma where the ratio equals to ~0.45 and for less sharp-edged tips. In opposite manner less intense circular flows in wake region may result in maximum accelerating currents closer to island's tip [31]. The southern tip of Stroma presents an asymmetry. At peak ebb phase (04/10/2001 3:20) currents with westward direction face a more-sharp edged tip, in comparison to currents flowing eastward at peak flood phase (04/10/2001 9:20). In effect ebb circular flows which form inside the westward wake region of Stroma are higher (up to 1.53 ms^{-1}, at the surface layer) in comparison to those observed inside the eastward wake region (up to 1.02 ms^{-1}, at the surface layer) at flood phase (Fig. 12). In opposite manner accelerating flood currents to the east reach a maximum of 4.7 ms^{-1}, at the surface layer closer to island's tip, in comparison to accelerating surface ebb currents of 4.34 ms^{-1} to the west (Fig. 11). As already observed and can be seen in Fig. 12, overall, surface and bottom current patterns vary in a similar manner however there

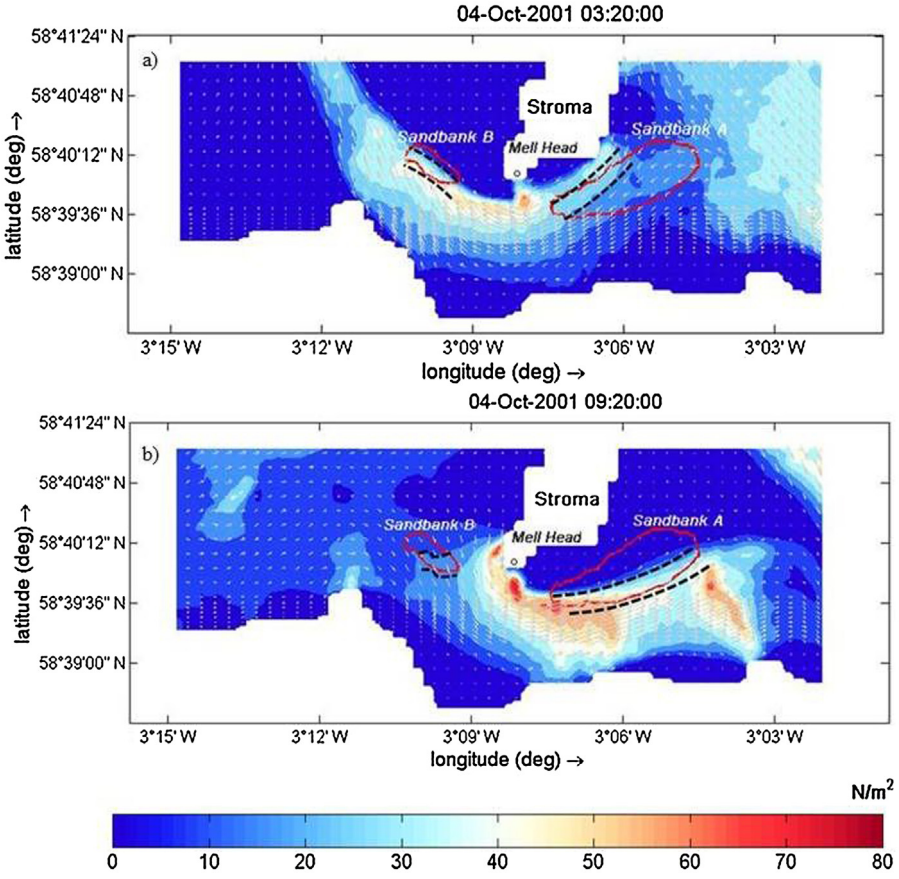

Fig. 14. Bed shear stresses (N/m^2) at maximum spring a) ebb (04/10/2001 3:20) and b) flood phase (04/10/2001 09:20) inside the Inner Sound channel. The colour bar indicates the magnitude of bed shear stresses and arrows indicate bed shear stresses direction. Red continuous lines denote the location of sandbanks A and B. Dashed black lines indicate pathways of maximum sediment transport capacity formed by maximum bed shear stress gradients on sandbanks A and B. (For interpretation of the references to color in this figure legend, the reader is referred to the web version of this article.)

are significant differences in their magnitudes at the surface and at sea bottom.

Fig. 12 proves that currents and topography interact locally and unevenly distribute current velocities around the tip of the Island of Stroma and further offshore inside Inner Sound where a notable tidal asymmetry between flood and ebb currents has been observed (see Section 4.1). The intensity of the velocity field is also unevenly distributed, throughout the water column around the areas where two sandbanks lie depending also on the proximity of sandbanks to island's tip. The east sandbank A lies closer to island's tip where bottom currents controlling sediment motions reach speeds of up to 2.8 ms^{-1} in comparison to speeds of less than 2.2 ms^{-1} on the west sandbank B located further offshore, over the spring tidal cycle (Fig. 12).

4.3. Residual tidal flows

Residual tidal currents are indicative of the mean flow patterns covering a period of few tidal cycles [32]. For a period covering the full spring tidal cycle (04/10/2001) modelled using Delft3D, the residual flow patterns were calculated in the Inner Sound. Residual flows are calculated based on the mean value of the horizontal velocities at the surface and bottom layer and at each point of the computational grid, following Bastos et al. [33]. It was found that the residual flows are significantly large, reaching up to 1.6 ms^{-1} and 1 ms^{-1} at the surface and bottom layers, in the leeward side of Stroma (Fig. 13). Strong residual eddies can be seen at the two sides of the Island of Stroma with the least velocities being observed at the center of those residual vortices (<0.2 ms^{-1}). A large anti-clockwise cyclonic eddy and a smaller scale clockwise anti-cyclonic eddy evolve eastwards and westwards of the Island of Stroma (Fig. 13). It seems that the residual circulation pattern mostly results from the significant asymmetry in horizontal tide found inside the channel.

It is possible that the center of the residual eddies will coincide with the presence of headland/island associated sandbanks [34]. As can be seen in Fig. 13, the presence of the east sandbank A coincides with the center of the cyclonic residual eddy. The west sandbank B is also observed within the center of the anticyclonic residual eddy. However, this observation is not proved to be true for all tidally dominated environments [33,35]. Several factors beyond the scope of this paper, studied in Signell and Harris [36] and Bastos et al. [33] will contribute to the relation between the location of sandbanks and the occurrence of the residual currents from few tidal cycles [33].

4.4. Tidal flows contribution to sandbanks sustenance

In view of principle island/headland sandbank formation concepts and main observations from sections above, further investigation has been attempted to explain tidal dynamics-sandbanks interactions inside Inner Sound channel. The predominant sandbank maintenance mechanisms are summarized in the tidal stirring concept [34,37], the stability analysis model [38,39] and models that predict sediment transport convergent zones formed by maximum ebb and flood sediment transport gradients, throughout the tidal cycle [40,36]. The seabed stability analysis model [38,39] has not been further considered in the present study, since it would

be more appropriate to explain the formation and maintenance of shallow linear sandbanks [41,42].

Following the tidal stirring concept, residual tidal currents generate secondary flows which converge and move sediments at the seabed and diverge at the surface. Opposite to stirring concept, peak ebb and flood flows are found to act as the maintenance mechanism of headland/island sandbanks in certain cases. Peak current flows induce areas of maximum bed shear stresses required to move sediments. Due to increasing gradients in ebb and flood shear stresses two distinct zones of maximum sediment transport capacity can be recognized. Such distinct zones lead to the formation of convergent pathways where sediments rest towards the center of the sandbanks [40,36].

It has been argued that the tidal stirring concept can be limited towards its application since the secondary flows are found to contribute only 5–15% of the main flows and the residual flow patterns are apparently weak to move sediments in comparison to peak tidal currents [43,44]. Numerical investigation in the present study reveals secondary flows which reach a maximum low value of 0.12 ms^{-1} at spring flood phase (04/10/2001, 9:20) [45]. Residual flows around two sandbanks (A, B) are also less than 20% of the main flows (Sections 4.1 & 4.3). The secondary currents are comparable in magnitude to those presented (0.13 ms^{-1}) by Geyer [44] in the vicinity of Gay Head, USA, and those measured (0.20–0.25 ms^{-1}) around Portland Bill, UK by Bastos et al. [43] and near Cape Levillain (Shark Bay), Western Australia by Berthot and Pattiaratchi [46].

The stirring concept can be considered to justify sediment transport patterns provided that the bed shear stresses required initializing sediment motions do not exceed their critical value which is not the case happening here in two sandbanks A and B in Inner Sound [40,41]. The Van Rijn [47] critical shear stress magnitude was calculated for both sandbanks based on information found on sediment size availability in Meygen [8]. The minimum critical shear stress on the east sandbank A was found to be equal to 2.21 N/m^2 and increases to 3.21 N/m^2 on the west sandbank B which are significantly exceeded during maximum ebb (04/10/2001, 3:20) and flood (04/10/2001, 9:20) flows (Fig. 14). As can be seen in Fig. 14 modelled maximum shear stress gradients form pathways of maximum sediment transport capacity on both sandbanks at ebb and flood phase. As a result of those findings the gradient model is proposed as the most appropriate approach to explain the presence of the observed sandbanks (A, B) inside Inner Sound channel, rather than the stirring concept.

5. Conclusions

In the present work Delf3D flow model was used to explore three dimensional hydrodynamics of Pentland Firth, Scotland, UK, Inner Sound Channel in particular. Sensitivity analysis was carried out to establish a detailed 3D flow model, which will reproduce the complex tidal flow regime in the Inner Sound channel, one of the most preferable areas for tidal energy extraction in the Pentland Firth. A detailed description of the hydrodynamic regime of the Inner Sound Channel was presented from simulations covering a spring-neap tidal cycle. At ebb phase a channel flow is formed and travels further offshore from the western side of the Island of Stroma. At flood phase, a tidal jet is formed to the south of the ebb channel flow and travels eastwards in a constrained path located in the middle part of Inner Sound. It is found that local flows interact with the Island of Stroma. As a result, enhanced circular flow patterns evolve in the west island wake region, at maximum ebb phase. Weaker circular flows can be observed in the east island wake region at maximum flood phase. The residual currents confirm the presence of a large anticlockwise cyclonic eddy eastwards and a smaller scale clockwise anticyclonic eddy westwards in the Inner Sound, resulting mostly from the significant asymmetry in tidal currents found inside the channel. Following main hydrodynamic features description in Inner Sound, the sediment transport gradient model which is driven by tidally dominant flows explained the existence of two island-associated sandbanks, observed in Inner Sound.

The results reveal that the location, integrity and the sustainability of the two sandbanks are closely linked with the existing flow regime of the Inner Sound. Therefore, any changes to the existing tidal regime as a result of tidal energy extraction may have some implications on the future of those sandbanks. Even though the present study is limited to Inner Sound channel, the models and methods developed here can be easily applied to any other site, given that adequate measurements are available to set up the model. Also, the findings of the study can be taken as a guide in formulating detailed investigations at other sites.

Acknowledgements

AC wishes to acknowledge College of Engineering of Swansea University and EA/Welsh Government funded Low Carbon Research Institute for the studentship provided to pursue her PhD research. HK acknowledges the support of EPSRC funded Terawatt (EP/J010170/1) and EcoWatt (EP/K012851/1) projects.

Appendix A. Supplementary data

Supplementary data associated with this article can be found, in the online version, at http://dx.doi.org/10.1016/j.apor.2017.04.008.

References

[1] European Ocean Energy Association. European ocean energy roadmap 2010–2050, http://www.erec.org/fileadmin/erec_docs/Documents/Publications/European%20Ocean%20Energy%20Roadmap_2010.pdf. 2012 (Accessed 6 May 14).
[2] Renewable UK, The Voice of Wind and Marine Energy. Wave and Tidal Energy in the UK Conquering Challenges, Generating Growth, 2013, http://www.renewableuk.com/en/publications/index.cfm/wave-and-tidal-energy-in-the-uk-2013. (Accessed 7 May 2014).
[3] The Crown Estate, UK Wave and Tidal Key Resource Areas Project. Technical Methodology Report, 2013, http://www.thecrownestate.co.uk/media/395109/uk-wave-and-tidal-key-resource-areas-technological-report.pdf. (Accessed 7 May 14).
[4] M.A. Shields, L.J. Dillon, D.K. Woolf, A.T. Ford, Strategic priorities for assessing ecological impacts of marine renewable energy devices in the Pentland Firth (Scotland, UK), Mar. Policy 33 (4) (2009) 635–642.
[5] S.P. Neill, J.R. Jordan, S.J. Couch, Impact of tidal energy converter (TEC) arrays on the dynamics of headland sandbanks, Renew. Energy 37 (1) (2012) 387–397.
[6] X. Sun, J.P. Chick, I.G. Bryden, Laboratory-scale simulation of energy extraction from tidal currents, Renew. Energy 33 (6) (2008) 1267–1274.
[7] S.J. Couch, I.G. Bryden, Tidal current energy extraction: hydrodynamic resource characteristics. in: Shenoi RA, (Ed.) Proceedings of the Institution of Mechanical Engineers, Part M: J. Engineering for Maritime Environment. Southampton, UK, University of Southampton; 2006, 220. p. 185–194.
[8] MeyGen, MeyGen Coastal Processes Modelling: Modelling Setups, Calibration and Results Incl. Addendum. A Final Report, MeyGen Coastal Processes, Singapore, 2012, Report No.: SG5390.
[9] P. Bowyer, G. Marchi, Tidal residual flows in the Pentland Firth, 9th European Wave and Tidal Energy Conference (2011).
[10] T.A.A. Adcock, S. Draper, G.T. Houlsby, A.G.L. Borthwick, On the tidal resource of the Pentland Firth, 4th International Conference on Ocean Energy (2012).
[11] S. Baston, R.E. Harris, Modelling the hydrodynamic characteristics of tidal flow in the Pentland Firth, 9th European Wave and Tidal Energy Conference (2011).
[12] M.G. Wells, G.J.F. Heijst, Van. Dipole formation by tidal flow in a channel, in: H.J. Gerhard, S.J.U. Wim (Eds.), Proceedings of the International Symposium on Shallow Flows; 2003 Jun 16–18, Delft, The Netherlands. Netherlands: Balkema Publishers, 2004, pp. 63–70.
[13] A. Chatzirodou, H. Karunarathna, D.E. Reeve, Investigation of deep sea shelf sandbank dynamics driven by highly energetic tidal flows, Mar. Geol. 380 (2016) 245–263.
[14] G.R. Lesser, J.A. Roelvink, J.A.T.M. Van Kester, G.S. Stelling, Development and validation of a three-dimensional morphological model, Coast. Eng. 51 (8–9) (2004) 883–915.

[15] N.A. Phillips, A co-ordinate system having some special advantages for numerical forecasting, J. Meteorol. 14 (1957) 184–185.
[16] Deltares, Delft3D-FLOW Simulation of Multi-dimensional Hydrodynamic Flows and Transport Phenomena, Including Sediments. A User Manual (Hydro-Morphodynamics) Version 3.15. Delft, Deltares, 2011.
[17] G.S. Stelling, J.J. Leendertse, Approximation of convective processes by cyclic AOI methods, Tampa Florida, USA. New York, NY, United States. ASCE Press, in: M.L. Spaulding, K. Bedford, A. Blumberg (Eds.), Estuarine and Coastal Modeling, Proceedings 2nd Conference on Estuarine and Coastal Modelling; 1991 November 13–15, 1992, 1992, pp. 771–782.
[18] NOAA National Geophysical Data Center. Coastline extracted (GSHHG). http://www.ngdc.noaa.gov/mgg/shorelines/shorelines.html, 2013. (Accessed 07 June 2013).
[19] NGDC, GEODAS-NG. Version 1.1.3.1 [software], 2017 [cited 2013 June 7]. Available from https://www.ngdc.noaa.gov/mgg/geodas/.
[20] T.A.A. Adcock, A.G.L. Borthwick, G.T. Houlsby, The open boundary problem in tidal basin modelling with energy extraction, 9th European Wave and Tidal Energy Conference (2011).
[21] S. Serhadlıoğlu, T.A.A. Adcock, G.T. Houlsby, S. Draper, A.G.L. Borthwick, Tidal stream energy resource assessment of the Anglesey Skerries, Int. J. Mar. Energy 3–4 (2013) e98–111, Special Issue – Selected Papers – EWTEC2013.
[22] G.D. Egbert, A.F. Bennett, M.G.G. Foreman, TOPEX/POSEIDON tides estimated using a global inverse model, J. Geophys. Res. 99 (C12) (1994) 24821–24852.
[23] S. Baston, R.E. Harris, D.K. Woolf, R.A. Hiley, J.C. Side, Sensitivity analysis of the turbulence closure models in the assessment of tidal energy resource in Orkney, 10th European Wave and Tidal Energy Conference (2013).
[24] T.A.A. Adcock, S. Draper, G.T. Houlsby, A.G.L. Borthwick, S. Serhadlıoğlu, The available power from tidal stream turbines in the Pentland Firth, Proc. R. Soc. A 469 (2013), no. 2157 20130072.
[25] D.T. Pugh, Tides, Surges and Mean Sea-level, John Wiley &Sons Ltd, UK, 1987.
[26] S.H. Salter, Correcting the under-estimate of the tidal-stream current resource of the Pentland Firth, 8th European Wave and Tidal Energy Conference (2009).
[27] M.C. Easton, D.K. Woolf, S. Pans, An operational hydrodynamic model of a key tidal-energy site: inner sound of stroma, Pentland Firth (Scotland, UK), 3rd International Conference on Ocean Energy (2010).
[28] C.J. Willmott, On the validation of models, J. Phys. Oceanogr. 2 (2) (1981) 184–194.
[29] Deltares, Delft Dashboard Computer Software, 2017, Version 64_r8621 [software]. [cited 2013 May 15] Available from https://publicwiki.deltares.nl/display/OET/DelftDashboard.
[30] L.M. Goddijn-Murphy, D.K. Woolf, M. Easton, Current patterns in the inner sound (Pentland firth) from underway ADCP data, J. Atmos. Ocean. Technol. 30 (1) (2013) 96–111.
[31] L. White, E. Wolanski, Flow separation and vertical motions in a tidal flow interacting with a shallow-water island, Estuar. Coastal Shelf Sci. 77 (2008) 457–466.
[32] N. Imasato, What is tide-induced residual current, J. Phys. Oceanogr. 13 (1983) 1307–1317.
[33] A.C. Bastos, M.B. Collins, N.H. Kenyon, Water and sediment movement around a coastal headland: portland Bill, Southern UK, Ocean Dyn. 53 (3) (2003) 309–321.
[34] R.D. Pingree, The formation of the Shambles and other banks by tidal stirring of the seas, J. Mar. Biol. Assoc. U. K. 58 (01) (1978) 211–226.
[35] A. Berthot, C.B. Pattiaratchi, Maintenance of headland associated linear sandbanks: modelling the secondary flows and sediment transport, Ocean Dyn. 55 (2005) 526–540.
[36] R.P. Signell, C.K. Harris, Modeling sand bank formation around tidal headlands, in: M.L. Spaulding, A.F. Blumberg (Eds.), Proceedings of the 6th International Conference on Estuarine Coastal Modeling; 1999 November 3–5, New Orleans, LA, USA., Reston, VA, United States ASCE, 2000, pp. 209–222.
[37] R.D. Pingree, L. Maddock, The tidal physics of headlands flows and offshore tidal bank formation, Mar. Geol. 32 (1979) 269–289.
[38] J.M. Huthnance, On one mechanism forming linear sandbanks, Estuar. Coastal Shelf Sci. 14 (1) (1982) 79–99.
[39] J.M. Huthnance, On the formation of sandbanks of finite extent, Estuar. Coastal Shelf Sci. 15 (3) (1982) 277–299.
[40] A.C. Bastos, N.H. Kenyon, M. Collins, Sedimentary processes, bedforms and facies, associated with a coastal headland: portland bill, Southern UK, Mar. Geol. 187 (3–4) (2002) 235–258.
[41] K.R. Dyer, D.A. Huntley, The origin, classification and modelling of sand banks and ridges, Cont. Shelf Res. 19 (1999) 1285–1330.
[42] J. Lanckneus, G. De Moor, Bedforms on the middelkerke bank, southern North Sea, in: B.W. Flemming, A. Bartholoma (Eds.), Tidal Signatures in Modern and Ancient Sediments, Blackwell Science, Oxford, 1995, pp. 33–51.
[43] A.C. Bastos, D. Paphitis, M.B. Collins, Short-term dynamics and maintenance processes of a headland-associated sandbank: shambles bank, English Channel (UK), Estuar. Coastal Shelf Sci. 59 (1) (2004) 33–47.
[44] W.R. Geyer, Three-dimensional tidal flow around headlands, J. Geophys. Res. C1 (1993) 955–966.
[45] A. Chatzirodou, H. Karunarathna, Impacts of tidal energy extraction on sea bed morphology, in: P. Lynett (Ed.), Proceedings of 34th Conference on Coastal Engineering; 2014 June 15–20, Seoul, Korea. Red Hook, NY, United States; Curran Associates, 2, 2016, pp. 1485–1494.
[46] A. Berthot, C.B. Pattiaratchi, Field measurements of the three-dimensional current structure in the vicinity of a headland-associated linear sandbank, Cont. Shelf Res. 26 (2006) 295–317.
[47] L.C. Van Rijn, Principles of Sediment Transport in Rivers, Estuaries and Coastal Seas, Aqua Publications, The Netherlands, 1993.